ACS APPLIED MATERIALS & INTERFACES

www.acsami.org

Research Article

Band-Edge Engineering To Eliminate Radiation-Induced Defect States in Perovskite Scintillators

Xiang-Yang Liu,* Ghanshyam Pilania, Anjana Anu Talapatra, Christopher R. Stanek, and Blas Pedro Uberuaga

Cite This: *ACS Appl. Mater. Interfaces* 2020, 12, 46296−46305

Read Online

ACCESS | Metrics & More | Article Recommendations | Supporting Information

ABSTRACT: Under radiative environments such as extended hard X- or γ-rays, degradation of scintillation performance is often due to irradiation-induced defects. To overcome the effect of deleterious defects, novel design mitigation strategies are needed to identify and design more resilient materials. The potential for band-edge engineering to eliminate the effect of radiation-induced defect states in rare-earth-doped perovskite scintillators is explored, taking Ce^{3+}-doped $LuAlO_3$ as a model material system, using density functional theory (DFT)-based DFT + U and hybrid Heyd−Scuseria−Ernzerhof (HSE) calculations. From spin-polarized hybrid HSE calculations, the Ce^{3+} activator ground-state 4f position is determined to be 2.81 eV above the valence band maximum in $LuAlO_3$. Except for the oxygen vacancies which have a deep level inside the band gap, all other radiation-induced defects in $LuAlO_3$ have shallow defect states or are outside the band gap, that is, relatively far away from either the 5d[1] or the 4f Ce^{3+} levels. Finally, we examine the role of Ga doping at the Al site and found that $LuGaO_3$ has a band gap that is more than 2 eV smaller than that of $LuAlO_3$. Specifically, the lowered conduction band edge envelopes the defect gap states, eliminating their potential impact on scintillation performance and providing direct theoretical evidence for how band-edge engineering could be applied to rare-earth-doped perovskite scintillators.

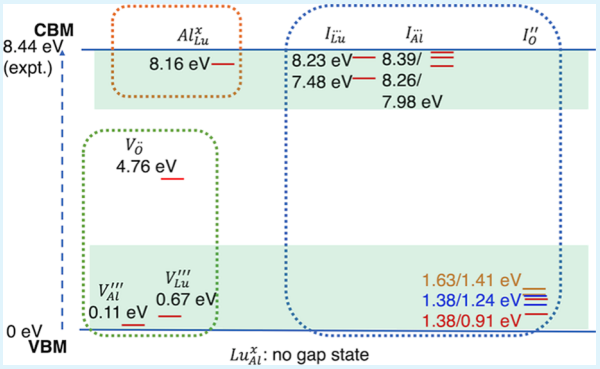

KEYWORDS: *first-principles calculations, perovskite scintillators, Ce^{3+} activator 4f level, radiation-induced defects, band-edge engineering*

INTRODUCTION

Scintillator materials are a class of materials that convert high-energy radiation such as X- or γ-rays to sharp pulses of visible or near-visible light. Such materials have widespread applications in global security and threat reduction, medical imaging, high-energy physics experiments, and space research.[1] Ideally, a scintillator for X- or γ-rays should have high light yield, fast response, stability under high-energy radiation, and efficient absorption of radiation, as well as be tuned to the specific application and detector system. Inorganic scintillators have received much attention, both historically and at present, because of the advantages of inorganic scintillators such as high light output and adsorption of γ-rays.[2] Among inorganic scintillators, Ce^{3+}-activated complex oxides are a particular class of materials noted for fast and bright scintillation properties because of the parity allowed and efficient 5d−4f transitions for Ce ions lying in the host band gap.[3−5] For these scintillators, a favorable electronic structure to enable efficient transportation and radiative recombination of charge careers is important for scintillation performance. Past theoretical efforts have focused largely on the electronic levels of 5d and 4f activator states and the associated chemical trends, as analyzed in great detail by Dorenbos.[6−8]

Defects are a common source of performance degradation. Defects can be intrinsic (i.e., thermal) or extrinsic, such as those formed during irradiation. Under radiative environments such as extended hard X- or γ-rays, degradation of scintillation performance is often due to irradiation-induced defects. This is because the defects created can form trap states that impact the scintillation performance. Thus, in addition to the thermodynamic and dynamic stability under irradiation, the ideal scintillator material should be able to withstand high doses of radiation without a significant degradation in performance. In this regard, to overcome the effect of deleterious defects, novel design mitigation strategies are needed to identify and design more resilient materials. There have been a few experimental works addressing the effects of high-energy X- or γ-rays radiation on scintillation performance for both inorganic scintillators[9−11] and organic scintillators.[12] However,

Received: July 22, 2020
Accepted: September 17, 2020
Published: September 17, 2020

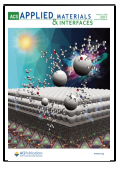

https://dx.doi.org/10.1021/acsami.0c13236
ACS Appl. Mater. Interfaces 2020, 12, 46296−46305

theoretical modeling of radiation effects on scintillators in general has been very limited. Further, more insight is needed into how to mitigate the effects of radiation-induced defects on performance in order to design improved scintillating materials.

In our previous theoretical work as well as collaborative experimental efforts,[13−15] it was shown that a doping strategy that allows for band gap engineering may be highly promising for the design of scintillators that can mitigate the effect of deleterious defects. A key aspect of this approach is that, by doping with species other than the activator element, the band edge can be shifted to envelop electron or hole traps caused by those defects. During this process, the level of the modified band edges should not be lower (for the conduction band minimum or CBM) than the Ce^{3+} activator excited state or higher (for the valence band maximum or VBM) than the Ce^{3+} activator ground state. In this way, the Ce^{3+} activator transition levels are still within the band gap, enabling scintillation. Such band gap engineering is expected to eliminate or reduce the effect of deleterious defects that act as sources of electron or hole traps.

In this paper, we build upon our previous efforts to explore the potential for band-edge engineering to eliminate the effect of radiation-induced defect states in rare-earth-doped perovskite scintillators. We explicitly show that these radiation-induced defect states would be swallowed by the shifting band edge.

Previous work, including our own, has shown how codoping can shift the band edges and swallow intrinsic trap states, enhancing the scintillating performance. However, the theoretical work failed to explicitly account for the defects, whether intrinsic or extrinsic, and demonstrate that the associated defect states are indeed subsumed into the bands. Here, we demonstrate, for the first time, that band-edge engineering of scintillators via codoping can eliminate the effects of radiation-induced defects and improve the performance and resilience of inorganic scintillators. This finding is important, as in principle, some of the defect states could shift with the bands and not get swallowed. Different from our previous theoretical works[13,15] involving density functional theory (DFT) calculations, the present calculations treat the material system in large supercells containing explicit defects or Ce^{3+} activator element, as well as dopants for band-edge engineering, thereby providing direct theoretical evidence for how band-edge engineering could be applied to rare-earth-doped perovskite scintillators.

We chose Ce^{3+}-doped $LuAlO_3$ (or commonly referred to as LuAP) as a model material system in this study. $LuAlO_3$/Ce is a promising scintillator for radiation detection because, in general, perovskite oxides have excellent γ-ray attenuation resulting from their high density and high effective atomic number.[16] There is strong experimental evidence that the presence of defect traps is a limiting factor in the scintillation performance of $LuAlO_3$/Ce,[17] thus making this theoretical effort more relevant to application. In addition, the $A^{3+}B^{3+}O_3$ perovskite structure of $LuAlO_3$ has a relatively simple crystal structure among complex oxides (e.g., compared to $A_3B_5O_{12}$ garnets), making it appealing for a computational study. Because of its promising scintillation properties, the defects in $LuAlO_3$ have been studied using empirical potentials[18,19] and DFT using both the local density approximation (LDA)[20,21] and the generalized gradient approximation (GGA).[22,23] In the present study, we employ DFT with both DFT + U as well as hybrid Heyd−Scuseria−Ernzerhof (HSE)[24,25] descriptions of the exchange−correlation interactions to understand the effect of radiation-induced defect states in LuAP.

METHODOLOGY

DFT + *U* Calculations. DFT + U calculations have been performed with the Vienna Ab initio Simulation Package (VASP)[26−28] using the projector augmented wave (PAW) method.[29,30] The DFT calculations employ the Perdew, Burke, and Ernzerhof (PBE)[31] GGA functional. The PAW−PBE pseudopotentials for the different elements in the current work include electron states $4f^{14}5s^25p^65d^1$ for Lu, $3s^23p^1$ for Al, $3s^23p^4$ for O, $5s^25p^65d^14f^1$ for Ce, and $3d^{10}4s^24p^1$ for Ga, resulting in a total of 25 (Lu), 3 (Al), 6 (O), 12 (Ce), and 13 (Ga) valence electrons, respectively. To describe the exchange and correlation effects and in particular to capture the intraband Coulomb repulsion among the 4f electrons, the simplified rotationally invariant DFT + U (or PBE + U, used interchangeably afterward) functional due to Dudarev et al.[32] is employed. For $LuAlO_3$ defect calculations not involving Ce^{3+}, spin-unpolarized calculations are performed because it is known that the $LuAlO_3$ crystal is nonmagnetic. Nevertheless, a ferromagnetic calculation for bulk $LuAlO_3$ was performed to test the assumption, resulting in nearly negligible magnetic moments for $LuAlO_3$. For defect calculations with supercells containing Ce^{3+}, spin-polarized calculations with Ce^{3+} magnetic moment are performed.

In the Dudarev version of DFT + U, only an effective U value is used (with J parameter set to 0). The U value of the Lu 4f states, as suggested by Ning et al.[22] and validated by our independent calculations, is set to U = 7 eV to match the experimental value of ∼−5 eV for the position of the Lu 4f band relative to the top of the valence band.[33] This value is larger than the U value used in DFT + U calculations of other Lu oxide phases, such as the value of 5.4 eV used for Lu_2O_3,[34] for instance.

For Ce 4f states, the U value is set to U = 2.5 eV. This is the same value used by Canning et al.[4] In their work, the calculated PBE + U 4f—VBM gaps are compared to precise measurements of seven Ce-doped oxides including Lu oxides ($Lu_2Si_2O_7$/Ce and Lu_2SiO_5/Ce) and are found to give satisfactory results. It is noted that in Canning et al.'s work,[4] $LuAlO_3$ is not specifically modeled, so the above choice of U value needs to be further validated. Compared to hybrid HSE calculations, we confirmed that this choice accurately describes the Ce states (see the Results section for a more detailed discussion on this). We would like to point out that the choice of U = 2.5 eV is very different from the value of 6 eV as suggested by Ning et al.[22]

The *Pnma* space group of $LuAlO_3$ crystal structure contains 20 atoms in its orthorhombic primitive supercell (see Figure S1 in the Supporting Information). For defect calculations, a 2 × 2 × 2 multiplication of the primitive cell is used, containing a total of 160 atoms, which is considered to be large enough for reliably modeling point defects. A 2 × 2 × 2 Monkhorst−Pack k-point mesh and a plane wave cutoff energy of 500 eV are used for the defect calculations. During structural relaxations, a Gaussian smearing (ISMEAR = 0 within VASP) with 0.05 eV broadening is used for electronic state occupations. The force relaxation criteria are set to 0.03 eV/Å. For projected density of state (pDOS) calculations, the tetrahedron method with Blöchl corrections (ISEMAR = −5) is used with a Γ-centered k-point mesh.

https://dx.doi.org/10.1021/acsami.0c13236
ACS Appl. Mater. Interfaces 2020, 12, 46296−46305

In the DFT + U calculations, one persistent issue is related to orbital ordering; for example, as observed in UO_2,[35] metastable states may be obtained depending on which 5f orbital occupations are used to initiate the electronic self-consistency cycles and the degree of symmetry in the supercell. To address the issue of possible metastable energy states, we follow the "U-ramping" method proposed by Meredig et al.[36] Testing this procedure on a 20-atom bulk cell of $LuAlO_3$, we found the same result from "U-ramping" as compared to direct calculations without symmetry constraint. Thus, no special treatment regarding the DFT + U calculations and metastable states is made beyond removing symmetry constraints for all calculations.

Hybrid HSE Calculations. Both regular DFT and DFT + U calculations significantly underestimate the band gap of $LuAlO_3$; thus, there is a need to carry out hybrid HSE calculations to further improve the result. Hybrid density functionals include a portion of screened Hartree−Fock (HF) exchange to replace the GGA functional. For hybrid calculations, an HSE06-like functional[37] is used. In the HSE06 functional, the inverse screening length parameter ω is set to 0.2 $Å^{-1}$, and the HF exchange mixing constant α is set to 0.25. It is possible to tune the α value to match the experimentally measured band gap value. To match the experimentally measured band gap of $LuAlO_3$ of 8.44 eV,[38] the mixing parameter of HSE is tuned to 0.33, resulting in a hybrid calculated band gap of 8.46 eV. Komsa et al.[39] used this approach to study the tuning of band gaps, band edges, and defect levels. This approach is also applied in our previous work on Ce-doped $A^{2+}B^{4+}O_3$ perovskite compounds.[16] Overall, this approach provides a relatively straightforward way to improve the description of some properties of the electronic structure of materials described by hybrid functionals.

For hybrid HSE calculations, as in DFT + U calculations, sufficiently large 160-atom supercells are used in defect calculations. Considering the large supercell size in the much slower hybrid HSE calculations, in order to speed up the calculations, an effective k-point set consisting of (0 0 0), (0.5 0.5 0), (0 0.5 0.5), and (0.5 0 0.5) is used. Using such a k-point set yields essentially similar results compared to using a 2 × 2 × 2 Monkhorst−Pack k-point mesh (which often ends up with eight special k-points). Such an implementation accelerates hybrid HSE calculations without sacrificing the calculation quality because the HF part of the hybrid HSE calculations scales as n^3 with a number of special k-points n used. Unless specifically mentioned, the HSE calculations are carried out with the electronic relaxations using HSE, on top of a PBE + U relaxed geometry.

Interstitial Defects. It is well known that, for interstitial defects in complex oxides, it is not trivial to identify the defect configurations.[40−42] In the present work, we employ a Python package PyCDT[43] interfaced with the pymatgen[44] framework to generate possible interstitial sites in $LuAlO_3$. PyCDT uses the Interstitial Finding Tool (InFiT) introduced by Zimmermann et al.,[45] which is based on local structural motifs to identify possible interstitial sites in crystals. It has been successfully applied in the modeling of interstitial defects in Cr_2O_3.[46]

More often than not, the PyCDT-generated interstitial configurations have some of the atoms too close to each other for efficient DFT or DFT + U calculations. A special procedure is taken to overcome this problem. Specifically, once the possible interstitial configurations are identified, the defect supercells are first relaxed using empirical potentials for 10 conjugate gradient relaxation steps with mobile atoms constrained to a certain region around the interstitial defect. The interatomic potential employed is of Buckingham type, with potential parameters taken from a previous work on $LuAlO_3$.[18,47] Subsequently, further atomic relaxations are carried out by regular PBE and PBE + U calculations. In all cases, the results are reported for the lowest energy structure or multistructures if energies are close enough. Only nominal charge states are considered in all DFT calculations.

RESULTS

Bulk Properties. The orthorhombic *Pnma* primitive cell of $LuAlO_3$ containing 20 atoms is structurally optimized using PBE + U (Figure S1). As introduced in the Methodology section, the pseudopotential for Lu contains the 4f states as valence electrons. In earlier regular PBE calculations,[22] the pseudopotential for Lu treated the 4f states as core electrons because the Lu pseudopotential that contains the 4f states as valence electrons without Hubbard correction (+U) yields less satisfactory results for $LuAlO_3$. Presumably, the Lu 4f states were also not considered in previous LDA[20] calculations either.

In Table 1, the calculated lattice and internal parameters and band gaps are compared to earlier DFT results (PBE[22] and LDA[20]) and experiments. The lattice constants obtained from the present PBE + U calculation are slightly improved compared to PBE,[22] with better agreement compared to most recent experimental data measured at 19k from synchrotron powder diffraction experiments.[48] The internal parameters of Lu and O atoms in the orthorhombic *Pnma* primitive cell obtained from the present PBE + U calculations, however, display no improvement over either PBE or LDA; nevertheless, all give reasonable agreement with the experiment. This is in agreement with a similar trend in earlier DFT work on $YAlO_3$.[49] Notably, both PBE + U and PBE give substantially smaller (6.05 and 5.7 eV, respectively) band gaps compared to the experimentally measured band gap of 8.44 eV.[38] LDA predicted a similar band gap of 5.8 eV.[20] In this work, we are interested in the dilute limit of an otherwise isolated defect or dopant within the crystal structure of LuAP. Thus, we explicitly keep the volume constant. Although it is known that even small amounts of doping can change the

Table 1. Calculated Lattice Constants, Internal Parameters of Lu and O Atoms in the Orthorhombic *Pnma* Primitive Cell, and the Band Gap of $LuAlO_3$ from the Present PBE + U Calculations As Compared to Earlier DFT Results and Experiments

	PBE + U	PBE[22]	LDA[20]	expt.[48]
a (Å)	5.310	5.369		5.329
b (Å)	7.305	7.345		7.293
c (Å)	5.042	5.113		5.097
Lu x	0.0659	0.0653	0.0659	0.0630
Lu z	0.9819	0.9830	0.9824	0.9843
O1 x	0.4602	0.4673	0.4685	0.474
O1 z	0.1126	0.1020	0.1021	0.089
O2 x	0.3040	0.3007	0.2999	0.303
O2 y	0.0575	0.0526	0.0528	0.0503
O2 z	0.6938	0.6972	0.6986	0.7031
band gap (eV)	6.05	5.7	5.8	8.44[a]

[a]Value taken from ref 38.

https://dx.doi.org/10.1021/acsami.0c13236
ACS Appl. Mater. Interfaces 2020, 12, 46296−46305

space group of the associated perovskite,[49] we are not interested in that regime in the current work.

For hybrid calculations, HSE06 (with $\alpha = 0.25$) gives a band gap of 7.86 eV. Thus, hybrid predictions are in close agreement with the experimental band gap while further tuning of the HF exchange mixing constant α from 0.25 to 0.33 matches the experimental band gap. The mBJ method[50] is also known to accurately predict the band gap of bulk solids;[51] however, much less is known about its applicability to defects such as dopants—while examining the accuracy of mBJ for defects and dopants is certainly of great interest, it is beyond the scope of the current work. For the rest of the paper, HSE (not HSE06) indicates that $\alpha = 0.33$ was used.

Determination of Ce^{3+} 4f Level. The scintillation performance of Ce-activated scintillators is decisively related to the 5d−4f transition of Ce dopants within the matrix, which leads to the emission of scintillation light through radiative recombination. In addition, the position of defect levels relative to the 4f and 5d transition levels also dictates the nature of possible trapping mechanisms in the host that can quench or reduce the transfer of energy from the incident radiation to the activator sites.[52] The 4f ground state of Ce^{3+} is usually harder to determine experimentally, while the energy difference between the 5d excited states and 4f ground state can be accurately measured from luminescence experiments.[33] Thus, there is a larger uncertainty associated with the determination of the 4f levels.

The 4f ground state of the activator dopant Ce^{3+} in scintillator perovskites is typically atomic-like and highly localized.[4,16] It was also demonstrated earlier that the occupied 4f band position relative to the VBM inside the band gap has an almost linear relationship with the applied Hubbard + U value in PBE + U calculations[22] (in ref 22, the Hubbard term was applied to Ce only, not to Lu. However, this trend does not expect to change if the Lu Hubbard term is included). Indeed, in that work,[22] the U value used (6 eV) was determined by matching the PBE + U predicted occupied 4f band position to a quoted experimental estimation that the Ce^{3+}-occupied 4f band position is approximately 1 eV above VBM.[33] We find that such a conclusion has two concerning issues:

(1) The 6 eV U value derived is significantly different from the U = 2.5 eV used by Canning et al.;[4] and

(2) In the Dorenbos model,[6] the 4f ground state of Ce^{3+} is predicted to be ∼3.5 eV (reading from Figure 4 of ref 6) above the VBM in $LuAlO_3$, which is different from the ∼1 eV estimation from the experiment.[33] Neither value comes directly from experimental measurements. In the Dorenbos model,[6] the prediction is based on the U(6,A)—4f electron binding energy difference between Eu^{2+} and Eu^{3+} in a given environment A, which is determined experimentally.[8] (Note that this U is different from the U in DFT + U.) In the case of ∼1 eV estimation from the experiment,[33] the estimation is inferred indirectly from the measured 4f level of Ce^{3+} in $CeAlO_3$.[33]

Spin-polarized hybrid HSE calculations (with $\alpha = 0.33$) are carried out with the goal of elucidating the positions of these states. The supercell is sufficiently large, containing 160 atoms, with one of the Lu atoms replaced by a Ce atom. The initial atomic relaxations are carried out using PBE + U. The structurally converged configuration is then further ionically relaxed using the HSE functional with a single Γ point k-point. A check of the relaxed configuration with a 4 k-point set yields slightly higher residual atomic forces, with a maximum force of 0.07 eV/Å. As shown in the Supporting Information, Figure S2, the Ce^{3+}-occupied 4f band position in $LuAlO_3$ predicted from hybrid HSE simulations is not very sensitive to the residual atomic forces if they are below 0.2 eV/Å. The 4f level of Ce^{3+} is determined to be 2.81 eV above the VBM in $LuAlO_3$. This value is reasonably close to the ∼3.5 eV from the Dorenbos model,[6] suggesting that it is the more accurate value.

From photoluminescence experiments, it is identified that there are five split 5d levels of Ce^{3+} responsible for photoadsorption peaks from 5d−4f transitions of Ce^{3+} in $LuAlO_3$.[33] The wavelengths of these optical peaks range from 32,890 to 46,210 cm^{-1}. This is used to determine the 5d levels of Ce^{3+}. As shown in Figure 1, with the calculated 4f level of

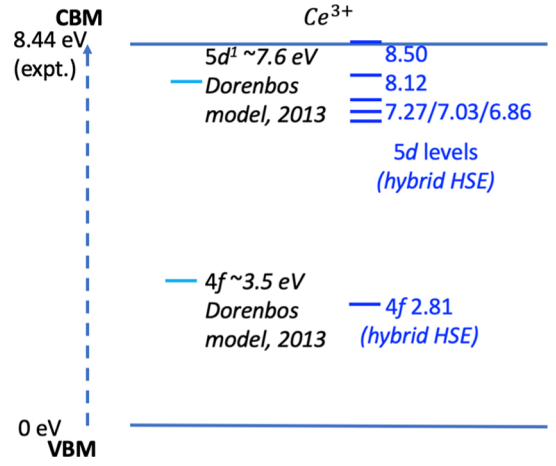

Figure 1. Schematic illustrating the hybrid HSE-calculated 4f and associated 5d levels of Ce^{3+} in $LuAlO_3$. The values from the Dorenbos model (ref 6) are also shown for comparison.

Ce^{3+}, one additional effect is that all calculated 5d levels of Ce^{3+} (using the sum of the calculated 4f state level and the experimentally measured 5d → 4f level transitions) are essentially below or at the CBM, while in the Dorenbos model, some of the higher 5d levels of Ce^{3+} are substantially higher than the CBM in $LuAlO_3$. In principle, the 5d levels below the CBM should give more substantial optical peaks than if they are well within the conduction band (CB). This result further supports the accuracy of our calculations.

Radiation-Induced Defects. In considering the types of defects that might be generated under irradiation, we consider different types of point defects, including Lu, Al, and O vacancies; Lu, Al, and O interstitials; and Lu_{Al} and Al_{Lu} antisite defects. Here, the A_B antisite defect indicates that an atom of type A resides on a site of composition B in the perfect crystal. The consideration of defect clusters or defect pairs is excluded for simplicity—we only consider isolated point defects at this time. Because the radiation-induced defects are expected to be generated under nonequilibrium conditions, the energetics of defects such as formation energies do not play a dominant role and thus are not explored further. Instead, we focus on the electronic structure of these defects, which will reveal how the defects impact scintillation performance and are relevant for band-edge engineering.

Because DFT + U substantially underestimates the band gap of $LuAlO_3$, one challenge is the possible prediction of defect

https://dx.doi.org/10.1021/acsami.0c13236
ACS Appl. Mater. Interfaces 2020, 12, 46296−46305

states within the corrected band gap without resulting into more expensive hybrid HSE calculations for every defect case. Through band structure calculations, we confirm that $LuAlO_3$ has a direct band gap. We tested the "scissor operation" procedure, a rigid upward shift of the DFT CB which, though empirical, is a widely used procedure,[53,54] using the Al_{Lu} antisite defect as a test case. In "scissor operation", the position ΔE of the energy of a defect state due to the incorrect band gap E^0_{gap} is simply a scaling of the state's energy in the incorrect description ΔE^0 by the correct band gap $E_{gap}{}^1$ via the relation

$$\Delta E = \Delta E^0 \times E_{gap}{}^1/E^0_{gap} \quad (1)$$

In our case, the defect state is scaled proportionally along with the band gap from DFT + U to the experimental band gap. We use a hybrid HSE06 calculation as a benchmark here. If this approach is successful, "high-throughput" (or automated) computations of these types of properties could be carried out.

In Figure 2a, the projected electron density of states, or pDOS, of the Al_{Lu} antisite defect in $LuAlO_3$ from PBE + U calculations is shown. The CB is dominated by the Lu 5d states, and the valence band is dominated by the O 2p states. The defect gap state has a peak at 5.85 eV above the VBM, mainly comprising the Al 3s states. There is also an appreciable Lu 4f and 5d character near the valence band edge, implying that these states can also participate in valence bond formation. Indeed, our separate calculations show that the energy cost of forming an Al_{Lu} antisite is different in PBE + U than in pure PBE calculations, suggesting the importance of including Lu 4f states in PBE + U (see the Supporting Information). In Figure 2b, the pDOS of the Al_{Lu} antisite defect in $LuAlO_3$ from HSE06 is shown, with similar features as in PBE + U calculations. The gap state has a peak at 7.62 eV above the VBM. This compares well with the "scissor operation" corrected gap-state position of 7.60 eV above the VBM. These values are also listed in Table 2.

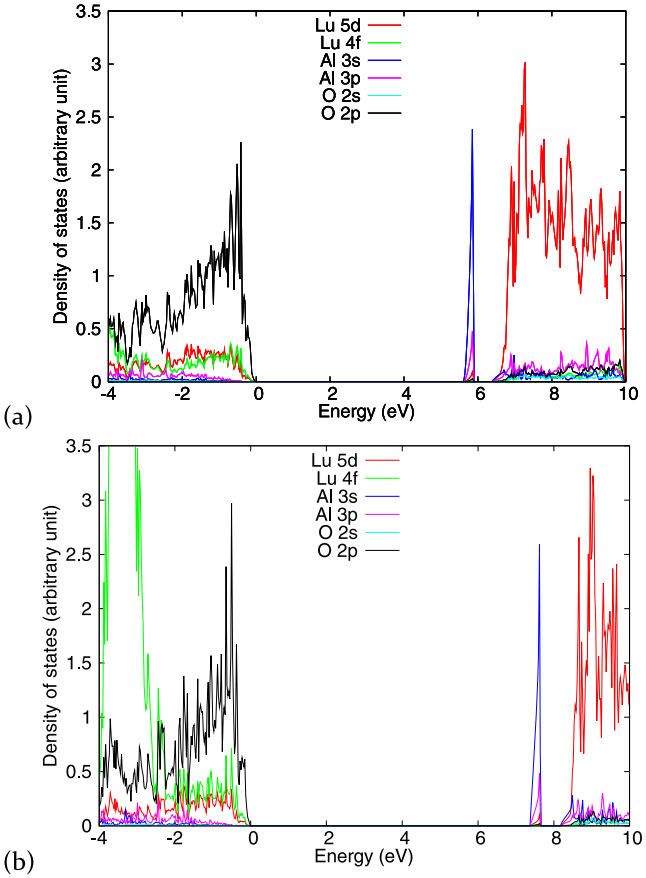

Figure 2. Projected electron density of states of the Al_{Lu} antisite defect in $LuAlO_3$ from (a) PBE + U and (b) HSE06.

Table 2. Calculated Gap-State Position and after "Scissor Operation" Gap-State Position of PBE + U Compared to That of HSE06 Results for the Al_{Lu} Antisite Defect[a]

	PBE + U (eV)	HSE06 (eV)	expt. (eV)
gap state	5.85	7.62	
after "scissor operation"	7.60		8.16

[a]The experimental band gap is also listed.

As an alternative approach to directly identifying defect states from the pDOS, it is also possible to determine the charge-state transition levels, which is based on the thermodynamics of a defect as a function of charge state and the Fermi level, as has been done in the study of photovoltaic materials.[55,56] This prior work has shown that some charge states can exhibit deeper defect states within the gap than revealed here. For each type of defect, we have only considered the nominal (full formal) charge state, as this is typically the dominant charge state encountered in nonequilibrium conditions such as irradiation, as described in a previous work on defect evolution in irradiated uranium dioxide.[57,58] Further, the approach outlined in ref 55 requires a full thermodynamic treatment, including the consideration of chemical potential references, that is beyond the scope of the current work.

Having validated the "scissor operation" approach, now we can proceed with using DFT + U calculations with scaling to the experimentally determined band gap of $LuAlO_3$ to assess the defect states associated with all of the point defects in the system. In Figure 3, the gap states of various defects are listed and marked within the band gap.

Of these defects, the antisite defect Lu_{Al} does not have any gap state, indicating that the induced defect states are well within the CB. Lu and Al interstitials (see Figures S3 and S4) have gap states near the CBM, similar to Al_{Lu}. For oxygen interstitials (see Figure S5), the defect states are close to the VBM, similar to the behavior seen for Lu and Al vacancies. These states are relatively far away from either the $5d^1$ or 4f Ce^{3+} levels. Therefore, there is a good opportunity to apply band-edge engineering to eliminate the effect of these defect states on carrier traps. That is, by shifting the CBM and/or VBM by the appropriate doping, those edges can be lowered and/or raised, respectively, to encompass those defect states without perturbing the activator levels.[13]

The only exception is the oxygen vacancy gap state, which is a deep level close to the mid gap. Such a deep level is not uncommon. In terms of Ce-doped perovskite scintillation performance, the deep level effect is not totally clear; however, we expect that these defect states have less impact on the Ce^{3+} 5d−4f transitions for the reason that it is far away from the conduction or valence bands.

Dopant Search and Ga Effect. From the results presented in Figure 3, we find that point defects such as Lu

https://dx.doi.org/10.1021/acsami.0c13236
ACS Appl. Mater. Interfaces 2020, 12, 46296−46305

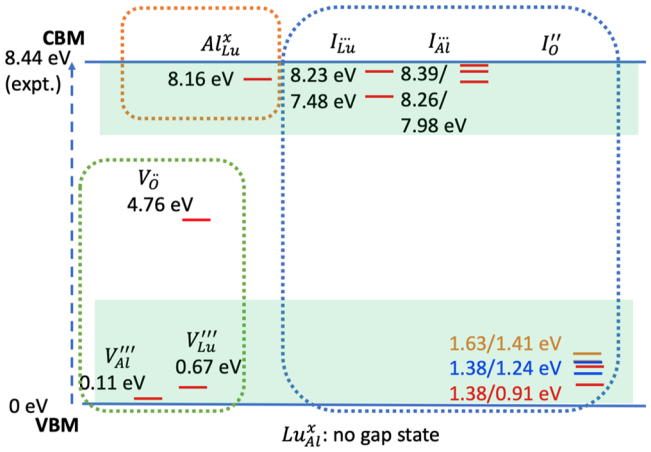

Figure 3. Schematic showing the defect-induced gap states in $LuAlO_3$. This is the picture after applying "scissor operation" to DFT + U values, scaling them to the experimental band gap. The dashed boxes simply group different classes of defects (antisites, vacancies, and interstitials). In the oxygen interstitial case, each defect configuration has two gap states, so different colors are used to have better clarity. The light-green-shaded areas indicate the region from band edges to ground-state 4f or to the lowest excited 5d ($5d^1$) level of Ce^{3+} in $LuAlO_3$, highlighting defect states that, in principle, could be subsumed into the bands while still keeping the activator states within the gap.

and Al interstitials and Al_{Lu} antisite defects lying just below the CB edge can potentially act as electron trap states and, thereby, adversely affect the scintillation performance in Ce-doped $LuAlO_3$. Use of chemical doping as a possible mitigation strategy to either alleviate or completely eliminate the effect of these unfavorable defect states on scintillation performance requires identification of a suitable chemical dopant species, which, when substituted in either the Lu or Al cation sublattices, leads to lowering of the bulk CBM to "engulf" the undesired defect states. To identify suitable A- or B-site substitutional dopant species across the periodic table, we look at various $XAlO_3$ or $LuYO_3$ compound chemistries reported in the Materials Project database[59] that are stable or near stable (energy above hull ΔE_{hull} < 100 meV) in a perovskite-type crystal structure with a *Pnma* space group. Note that this criterion naturally accounts for factors such as a similar atomic size and nominal charge state for the substitutional dopant X (Y) with respect to Lu (Al). Furthermore, because a partial doping of this chemical species should significantly lower the CBM (by about 1 eV), we require that the PBE band gap of these bulk chemistries should be significantly lower than that of the host $LuAlO_3$.

Given these constraints—that the identified substitutional elements that should likely preserve the *Pnma* phase even with a large amount of doping and at the same time bringing down the CB edge significantly (without going to a metallic state)—our substitutional dopant search analysis shows that, for X = Sc, Sm, and Gd, the A-site substitution is likely to be thermodynamically favorable (ΔE_{hull} = 28, 0, and 8 meV, respectively) and all of these dopants lead to a significant lowering of the CB edge with respect to $LuAlO_3$ (with PBE band gaps of 4.6, 4.8, and 3.2 eV, respectively, compared to the 5.7 eV band gap of $LuAlO_3$). The problem with other rare-earth elements seems to be that they lead to very similar band gaps, which would lead to a slower or no lowering of the CB edge with respect to the host upon substitutional doping. For example, the PBE band gaps of $XAlO_3$ with X = Er (5.80 eV), Tm (5.77 eV), Dy (5.72 eV), and Tb (5.60 eV) are very close to that of the host $LuAlO_3$. Yttrium also exhibits a similar behavior to these rare-earth elements (with $YAlO_3$ or YAP PBE band gap being close to 5.5 eV). It is worth noting that, as a result of different local chemical environments and bonding, going from LuAP to YAP, the bulk PBE band gap change is much smaller (~0.2 eV) as compared to a similar chemical change in garnets: going from $Lu_3Al_5O_{12}$ to $Y_3Al_5O_{12}$ results in a ~0.5 eV shift in the band edge. Thus, we expect yttrium to be a less-effective substitutional dopant in lowering the CB edge when it comes to perovskites.

Following the same analysis, for the B-site, the most promising candidate dopant species identified are Y = Sc and Ga (with ΔE_{hull} = 64 and 54 meV, respectively), exhibiting bulk *Pnma* $LuYO_3$ PBE band gaps of 4.45 and 3.64 eV, respectively.

Going forward, out of the six potential substitutional dopant choices identified above as promising for modifying the band edge of $LuAlO_3$, we choose Ga doping at the Al site to demonstrate our approach for the following reasons:

(1) While all other chemistries belong to rare earths, Ga stands out because of its chemically distinct nature and 4s and 4p valence electrons.

(2) The 4f−4f transitions accessible in a new lanthanide dopant might lead to additional complications in the scintillation process (although this should not be a problem with Lu^{3+} with the 4f shell completely full).

(3) Sc^{3+} is predicted to have a preference for occupying both the A- and B-sites and therefore the doped configurations can be difficult to control and characterize in experiments.

To investigate the effect of Ga doping on the band structure and the potential for band-edge engineering in this system, we consider complete substitution of Ga for Al in $LuAlO_3$, leading to $LuGaO_3$. The orthorhombic form of $LuGaO_3$ in the *Pnma* space group has been successfully synthesized before,[60] although the lowest energy structure is a hexagonal form. Although we realize that the Ga dopant concentration in $LuAlO_3$ in experiments is rather small,[61] the advantage of studying the Ga effect in fully substituted $LuGaO_3$ is that one need not resort to exhaustive alloy plus defect configurations in medium or dilute Ga-doped $LuAlO_3$. We expect by studying the effect of Ga by considering $LuGaO_3$, a useful trend can be identified.

In Figure 4a, the total density of states calculated using hybrid HSE for orthorhombic perovskite $LuGaO_3$ is compared to that for $LuAlO_3$. In addition, the hybrid HSE-calculated pDOS of $LuGaO_3$ is shown in Figure 4b. The calculated band gap is 6.07 eV, which is substantially smaller (by more than 2 eV) than that of $LuAlO_3$. The same band gap calculated from DFT + U is 3.7 eV. One striking difference of the $LuGaO_3$ pDOS as compared to that of $LuAlO_3$ is that, at the CB edge, the dominant states are Ga 4s states, rather than the Lu 5d states, which are dominant at the CB edge of $LuAlO_3$. We will show that the change of the dominant states at the CB edge as well as the associated chemical species makes a huge impact on the nature of defect-induced states.

Now we consider the electronic structure of defects in $LuGaO_3$ using PBE + U. In Figure 5, the pDOS of the Lu interstitial in $LuGaO_3$ is shown (we assume the same defect structures as found above for $LuAlO_3$). In this figure, the

https://dx.doi.org/10.1021/acsami.0c13236
ACS Appl. Mater. Interfaces 2020, 12, 46296−46305

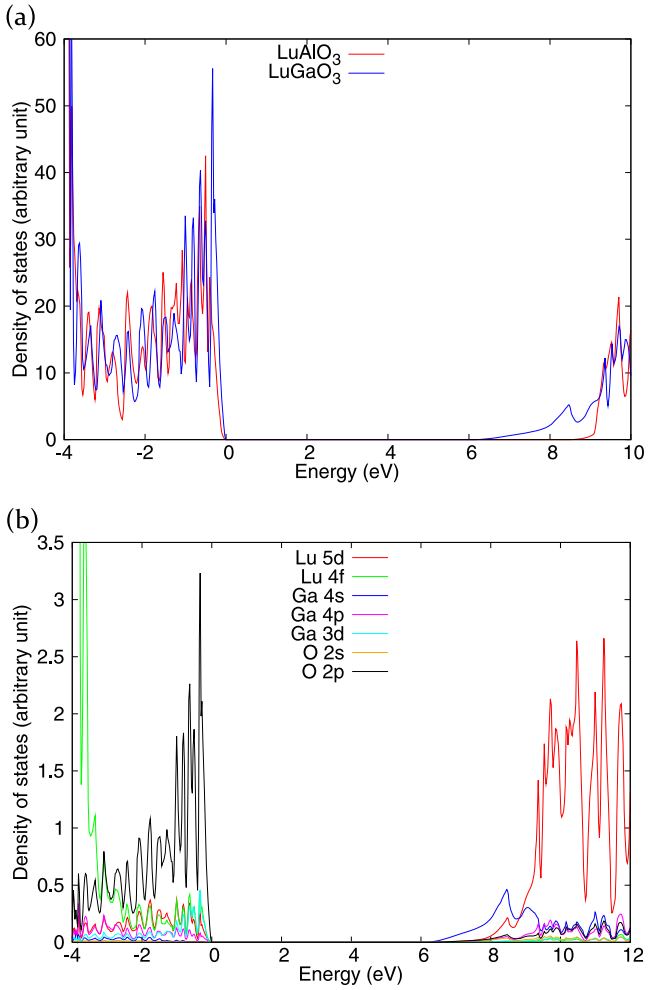

Figure 4. (a) Total density of states of $LuAlO_3$ and $LuGaO_3$ from hybrid HSE. (b) Projected electron density of states of $LuGaO_3$ from hybrid HSE.

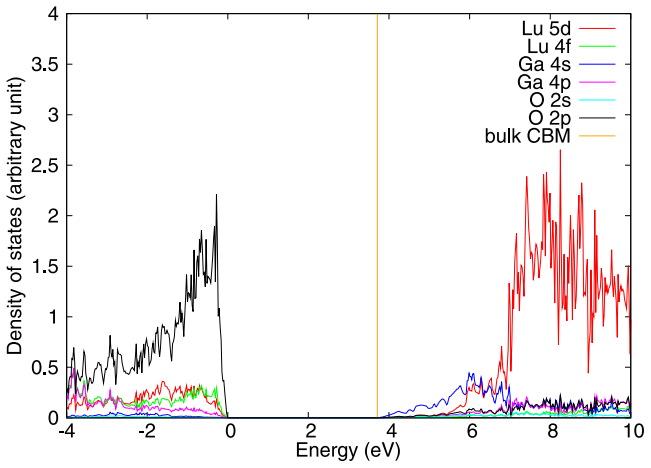

Figure 5. Projected electron density of states of Lu interstitial in $LuGaO_3$ from PBE + *U*.

orange-colored vertical line is used to mark the CBM band edge in pure bulk $LuGaO_3$. As expected, there is a slight lowering of the CB due to the defect; however, strikingly different from the cases of $LuAlO_3$ defects, the density of states below the pure bulk $LuGaO_3$ CBM is negligibly small. Indeed, the lowered CB edge envelopes the defect states which otherwise reside in the band gap in the case of $LuAlO_3$. PBE + *U* calculations have also been carried out for Ga interstitial, Lu_{Ga}, and Ga_{Lu} antisite defect cases (see Figures S6 and S7 in the Supporting Information). The pDOS in the former two cases look very similar to the Lu interstitial case, with the defect states essentially completely in the (pure bulk $LuGaO_3$) CBs. In the case of the Ga_{Lu} antisite defect, the defect-induced density of states below the pure bulk $LuGaO_3$ CBM is, while non-negligible, fairly small (and far away from its peak, see Figure S7 in the Supporting Information), implying a mostly delocalized behavior.

These results highlight the drastic changes in the electronic structure when Ga replaces Al in $LuAlO_3$. It is indeed possible that, by doping with elements other than the activator element, the band edge can be shifted to envelop the electron or hole traps due to radiation-induced defects, as demonstrated in the $LuGaO_3$ defect cases. However, we expect that all of the Ce^{3+}-excited 5d states may fall in the CB because of the extremely high amount of Ga doping represented by $LuGaO_3$, so the optimal doping would depend on balancing these factors. Thus, while these results highlight the promise of codoping to eliminate the traps associated with radiation-induced defects, further work is needed to identify the precise doping levels that will leave the activator states unaffected.

DISCUSSION

Although in this study we have specifically focused on CB-edge engineering to illustrate our chemical doping-based approach to alleviate the deleterious effects of shallow defect states on scintillation performance, a similar strategy can also be adopted toward valence band-edge engineering. For instance, because the O 2p states predominantly contribute to the VBM, moving to heteroanionic perovskite chemistries (e.g., partial doping with sulfur (S), or even resorting to a chemically similar oxynitride chemistry) could be an alternative pathway to get rid of the hole trap states in oxide scintillators for improved performance. Furthermore, more implicit strategies can also be considered where rather than targeting to tailor the electronic structure of the host compound directly, one relies on thermodynamic effects to reduce the concentration of the deleterious defects (more traditional defect engineering approaches). For example, an aliovalent cation substitutional dopant, such as Mg^{2+}, is likely to promote oxygen vacancies while suppressing the formation of oxygen interstitials and cation vacancies (i.e., hole trapping defects that form states near the VBM) and thereby leading to better performance via improved hole mobilities.

CONCLUSIONS

To conclude, we explore the potential for band-edge engineering to eliminate the effect of radiation-induced defect states in rare-earth-doped perovskite scintillators, taking Ce^{3+}-doped $LuAlO_3$ as a model material system. DFT + *U* and hybrid HSE calculations are carried out to understand the nature of gap states produced by radiation-induced defects. The primary results of this study include the following:

(a) Spin-polarized hybrid HSE calculations elucidate the Ce^{3+} activator ground-state 4f position inside the band gap, which is determined to be 2.81 eV above the VBM in $LuAlO_3$. This value is close to the ~3.5 eV from Dorenbos' model.[6]

https://dx.doi.org/10.1021/acsami.0c13236
ACS Appl. Mater. Interfaces 2020, 12, 46296−46305

(b) Except for the oxygen vacancy which has deep level inside band gap, all other radiation-induced defects in $LuAlO_3$ have shallow defect states or states inside the CB, at least when they are fully charged. These states are relatively far away from either the $5d^1$ or 4f Ce^{3+} levels. Therefore, there is an opportunity to apply band-edge engineering to eliminate the effect of these defect states on carrier traps.

(c) The lowered CB edge in Ga-doped $LuAlO_3$ (represented by $LuGaO_3$) is found to essentially envelope the defect states which otherwise reside in the band gap of $LuAlO_3$.

Together, these results provide direct theoretical support that band-edge engineering via doping could be applied to rare earth perovskite scintillators to eliminate the deleterious effects of radiation-induced defects and thus improve their scintillation efficiency in damaging environments.

■ ASSOCIATED CONTENT

Supporting Information

The Supporting Information is available free of charge at https://pubs.acs.org/doi/10.1021/acsami.0c13236.

Primitive cell of $LuAlO_3$, Ce^{3+}-occupied 4f position in $LuAlO_3$ as a function of residual forces, Lu interstitial configuration in $LuAlO_3$, one of the two Al interstitial low-energy configurations in $LuAlO_3$, oxygen interstitial configuration in $LuAlO_3$, and pDOS of Ga interstitial in $LuGaO_3$ from PBE + U (PDF)

■ AUTHOR INFORMATION

Corresponding Author

Xiang-Yang Liu − *Materials Science and Technology Division, Los Alamos National Laboratory, Los Alamos, New Mexico 87545, United States;* orcid.org/0000-0003-4183-3802; Email: xyliu@lanl.gov

Authors

Ghanshyam Pilania − *Materials Science and Technology Division, Los Alamos National Laboratory, Los Alamos, New Mexico 87545, United States;* orcid.org/0000-0003-4460-1572

Anjana Anu Talapatra − *Materials Science and Technology Division, Los Alamos National Laboratory, Los Alamos, New Mexico 87545, United States*

Christopher R. Stanek − *Materials Science and Technology Division, Los Alamos National Laboratory, Los Alamos, New Mexico 87545, United States*

Blas Pedro Uberuaga − *Materials Science and Technology Division, Los Alamos National Laboratory, Los Alamos, New Mexico 87545, United States;* orcid.org/0000-0001-6934-6219

Complete contact information is available at: https://pubs.acs.org/10.1021/acsami.0c13236

Notes

The authors declare no competing financial interest.

■ ACKNOWLEDGMENTS

This work was supported by the Los Alamos National Laboratory (LANL) Directed Research and Development Program. LANL is operated by Triad National Security, LLC, for the National Nuclear Security Administration of the U.S. Department of Energy under contract no. DE-AC52-06NA25396.

■ REFERENCES

(1) Dujardin, C.; Auffray, E.; Bourret-Courchesne, E.; Dorenbos, P.; Lecoq, P.; Nikl, M.; Vasil'ev, A. N.; Yoshikawa, A.; Zhu, R.-Y. Needs, Trends, and Advances in Inorganic Scintillators. *IEEE Trans. Nucl. Sci.* **2018**, *65*, 1977−1997.

(2) Rodnyi, P. A. *Physical Processes in Inorganic Scintillators*; CRC Press: Boca Raton, 1997.

(3) Weber, M. J. Scintillation: Mechanisms and New Crystals. *Nucl. Instrum. Methods Phys. Res., Sect. A* **2004**, *527*, 9−14.

(4) Canning, A.; Chaudhry, A.; Boutchko, R.; Gronbech-Jensen, N. First-Principles Study of Luminescence in Ce-Doped Inorganic Scintillators. *Phys. Rev. B: Condens. Matter Mater. Phys.* **2011**, *83*, 125115.

(5) Martin, T.; Koch, A.; Nikl, M. Scintillator Materials for X-Ray Detectors and Beam Monitors. *MRS Bull.* **2017**, *42*, 451−457.

(6) Dorenbos, P. Determining Binding Energies of Valence-Band Electrons in Insulators and Semiconductors Via Lanthanide Spectroscopy. *Phys. Rev. B: Condens. Matter Mater. Phys.* **2013**, *87*, 035118.

(7) Dorenbos, P. The Electronic Level Structure of Lanthanide Impurities in Repo4, Rebo3, Realo3, and Re2o3 (Re = La, Gd, Y, Lu, Sc) Compounds. *J. Phys. Condens. Matter* **2013**, *25*, 225501.

(8) Dorenbos, P. Modeling the Chemical Shift of Lanthanide 4f Electron Binding Energies. *Phys. Rev. B: Condens. Matter Mater. Phys.* **2012**, *85*, 165107.

(9) Zhu, R. Y. Ultrafast and Radiation Hard Inorganic Scintillators for Future Hep Experiments. *18th International Conference on Calorimetry in Particle Physics (Calor2018)*, 2019; p 1162.

(10) Annenkov, A. N.; Auffray, E.; Chipaux, R.; Drobychev, G. Y.; Fedorov, A. A.; Géléoc, M.; Golubev, N. A.; Korzhik, M. V.; Lecoq, P.; Lednev, A. A.; Ligun, A. B.; Missevitch, O. V.; Pavlenko, V. B.; Peigneux, J.-P.; Singovski, A. V. Systematic Study of the Short-Term Instability of Pbwo4 Scintillator Parameters under Irradiation. *Radiat. Meas.* **1998**, *29*, 27−38.

(11) Yang, F.; Zhang, L.; Zhu, R.-Y. Gamma-Ray Induced Radiation Damage up to 340 Mrad in Various Scintillation Crystals. *IEEE Trans. Nucl. Sci.* **2016**, *63*, 612−619.

(12) Khachatryan, V.; Sirunyan, A. M.; Tumasyan, A.; Litomin, A.; Mossolov, V.; Shumeiko, N.; Van de Klundert, M.; Van Haevermaet, H.; Van Mechelen, P.; Van Spilbeeck, A.; Alves, G. A.; Alda, W. L.; Hensel, C.; Carvalho, W.; Chinellato, J.; Martins, C. D.; Figueiredo, D. M.; Herrera, C. M.; Nogima, H.; Da Silva, W. L. P.; Manganote, E. J. T.; Pereira, A. V.; Finger, M.; Finger, M.; Jain, S.; Khurana, R.; Adamov, G.; Tsamalaidze, Z.; Behrens, U.; Borras, K.; Campbell, A.; Costanza, F.; Gunnellini, P.; Lobanov, A.; Melzer-Pellmann, I. A.; Muhl, C.; Roland, B.; Sahin, M.; Saxena, P.; Hegde, V.; Kothekar, K.; Pandey, S.; Sharma, S.; Beri, S. B.; Bhawandeep, B.; Chawla, R.; Kalsi, A.; Kaur, A.; Kaur, M.; Walia, G.; Bhattacharya, S.; Ghosh, S.; Nandan, S.; Purohit, A.; Sharan, M.; Banerjee, S.; Bhattacharya, S.; Bhowmik, S.; Chatterjee, S.; Das, P.; Dewanjee, R. K.; Jain, S.; Kumar, S.; Maity, M.; Majumder, G.; Mandakini, P.; Patil, M.; Sarkar, T.; Saikh, A.; Sezen, S.; Juodagalvis, A.; Afanasiev, S.; Bunin, P.; Ershov, Y.; Golutvin, I.; Malakhov, A.; Moisenz, P.; Smirnov, V.; Zarubin, A.; Chadeeva, M.; Chistov, R.; Danilov, M.; Popova, E.; Rusinov, V.; Andreev, Y.; Dermenev, A.; Karneyeu, A.; Krasnikov, N.; Tlisov, D.; Toropin, A.; Epshteyn, V.; Gavrilov, V.; Lychkovskaya, N.; Popov, V.; Pozdnyakov, I.; Safronov, G.; Toms, M.; Zhokin, A.; Flacher, H.; Baskakov, A.; Belyaev, A.; Boos, E.; Dubinin, M.; Dudko, L.; Ershov, A.; Gribushin, A.; Kaminskiy, A.; Klyukhin, V.; Kodolova, O.; Lokhtin, I.; Miagkov, I.; Obraztsov, S.; Petrushanko, S.; Savrin, V.; Snigirev, A.; Andreev, V.; Azarkin, M.; Dremin, I.; Kirakosyan, M.; Leonidov, A.; Terkulov, A.; Bitioukov, S.; Elumakhov, D.; Kalinin, A.; Krychkine, V.; Mandrik, P.; Petrov, V.; Ryutin, R.; Sobol, A.; Troshin, S.; Volkov, A.; Adiguzel, A.; Bakirci, N.; Cerci, S.; Damarseckin, S.; Demiroglu, Z. S.; Dozen, C.; Dumanoglu, I.; Eskut, E.; Girgis, S.; Gokbulut, G.; Guler, Y.; Hos, I.; Kangal, E. E.; Kara, O.; Topaksu, A. K.; Kiminsu, U.; Oglakci, M.; Onengut, G.; Ozdemir, K.; Ozturk, S.;

Polatoz, A.; Cerci, D. S.; Tali, B.; Topakli, H.; Turkcapar, S.; Zorbakir, I. S.; Zorbilmez, C.; Bilin, B.; Isildak, B.; Karapinar, G.; Guler, A. M.; Ocalan, K.; Yalvac, M.; Zeyrek, M.; Gulmez, E.; Kaya, M.; Kaya, O.; Yetkin, E. A.; Yetkin, T.; Cankocak, K.; Sen, S.; Boyarintsev, A.; Grynyov, B.; Levchuk, L.; Popov, V.; Sorokin, P.; Borzou, A.; Call, K.; Dittmann, J.; Hatakeyama, K.; Liu, H.; Pastika, N.; Charaf, O.; Cooper, S. I.; Henderson, C.; Rumerio, P.; West, C.; Arcaro, D.; Gastler, D.; Hazen, E.; Rohlf, J.; Sulak, L.; Wu, S.; Zou, D.; Hakala, J.; Heintz, U.; Kwok, K. H. M.; Laird, E.; Landsberg, G.; Mao, Z.; Gary, J. W.; Shirazi, S. M. G.; Lacroix, F.; Long, O. R.; Wei, H.; Bhandari, R.; Heller, R.; Stuart, D.; Yoo, J. H.; Apresyan, A.; Chen, Y.; Duarte, J.; Spiropulu, M.; Winn, D.; Abdullin, S.; Chlebana, F.; Freeman, J.; Green, D.; Hare, D.; Hirschauer, J.; Joshi, U.; Lincoln, D.; Los, S.; Pedro, K.; Spalding, W. J.; Strobbe, N.; Tkaczyk, S.; Whitbeck, A.; Linn, S.; Markowitz, P.; Martinez, G.; Bertoldi, M.; Hagopian, S.; Hagopian, V.; Kolberg, T.; Baarmand, M. M.; Noonan, D.; Roy, T.; Yumiceva, F.; Bilki, B.; Clarida, W.; Debbins, P.; Dilsiz, K.; Durgut, S.; Gandrajula, R. P.; Haytmyradov, M.; Khristenko, V.; Merlo, J. P.; Mermerkaya, H.; Mestvirishvili, A.; Miller, M.; Moeller, A.; Nachtman, J.; Ogul, H.; Onel, Y.; Ozok, F.; Penzo, A.; Schmidt, I.; Snyder, C.; Southwick, D.; Tiras, E.; Yi, K.; Al-bataineh, A.; Bowen, J.; Castle, J.; McBrayer, W.; Murray, M.; Wang, Q.; Kaadze, K.; Maravin, Y.; Mohammadi, A.; Saini, L. K.; Baden, A.; Belloni, A.; Eno, S. C.; Ferraioli, C.; Grassi, T.; Hadley, N. J.; Jeng, G. Y.; Kellogg, R. G.; Kunkle, J.; Mignerey, A.; Ricci-Tam, F.; Shin, Y. H.; Skuja, A.; Tonjes, M. B.; Yang, Z. S.; Apyan, A.; Bierwagen, K.; Brandt, S.; Klute, M.; Niu, X.; Chatterjee, R. M.; Evans, A.; Frahm, E.; Kubota, Y.; Lesko, Z.; Mans, J.; Ruckstuhl, N.; Heering, A.; Karmgard, D. J.; Musienko, Y.; Ruchti, R.; Wayne, M.; Benaglia, A. D.; Medvedeva, T.; Mei, K.; Tully, C.; Bodek, A.; de Barbaro, P.; Galanti, M.; Garcia-Bellido, A.; Khukhunaishvili, A.; Lo, K. H.; Vishnevskiy, D.; Zielinski, M.; Agapitos, A.; Chou, J. P.; Hughes, E.; Saka, H.; Sheffield, D.; Akchurin, N.; Damgov, J.; De Guio, F.; Dudero, P. R.; Faulkner, J.; Gurpinar, E.; Kunori, S.; Lamichhane, K.; Lee, S. W.; Libeiro, T.; Undleeb, S.; Volobouev, I.; Wang, Z.; Goadhouse, S.; Hirosky, R.; Wang, Y.; Collaboration, C.-H. Dose Rate Effects in the Radiation Damage of the Plastic Scintillators of the Cms Hadron Endcap Calorimeter. *J. Instrum.* **2016**, *11*, T10004.

(13) Fasoli, M.; Vedda, A.; Nikl, M.; Jiang, C.; Uberuaga, B. P.; Andersson, D. A.; McClellan, K. J.; Stanek, C. R. Band-Gap Engineering for Removing Shallow Traps in Rare-Earth Lu3al5o12 Garnet Scintillators Using Ga3+ Doping. *Phys. Rev. B: Condens. Matter Mater. Phys.* **2011**, *84*, 081102.

(14) Nikl, M.; Yoshikawa, A.; Kamada, K.; Nejezchleb, K.; Stanek, C. R.; Mares, J. A.; Blazek, K. Development of Luag-Based Scintillator Crystals - a Review. *Prog. Cryst. Growth Charact. Mater.* **2013**, *59*, 47−72.

(15) Yadav, S. K.; Uberuaga, B. P.; Nikl, M.; Jiang, C.; Stanek, C. R. Band-Gap and Band-Edge Engineering of Multicomponent Garnet Scintillators from First Principles. *Phys. Rev. Appl.* **2015**, *4*, 054012.

(16) Pilania, G.; Yadav, S. K.; Nikl, M.; Uberuaga, B. P.; Stanek, C. R. Role of Multiple Charge States of Ce in the Scintillation of Abo(3) Perovskites. *Phys. Rev. Appl.* **2018**, *10*, 024026.

(17) Wojtowicz, A. J.; Szupryczynski, P.; Wisniewski, D.; Glodo, J.; Drozdowski, W. Electron Traps and Scintillation Mechanism in Lualo3 : Ce. *J. Phys. Condens. Matter* **2001**, *13*, 9599−9619.

(18) Stanek, C. R.; McClellan, K. J.; Levy, M. R.; Grimes, R. W. Defect Behavior in Rare Earth Realo3 Scintillators. *J. Appl. Phys.* **2006**, *99*, 113518.

(19) Stanek, C. R.; Levy, M. R.; McClellan, K. J.; Uberuaga, B. P.; Grimes, R. W. Defect Structure of Zro2-Doped Rare Earth Perovskite Scintillators. *Phys. Status Solidi B* **2005**, *242*, R113−R115.

(20) Singh, D. J. Antisite Defects and Traps in Perovskite Yalo3 and Lualo3: Density Functional Calculations. *Phys. Rev. B: Condens. Matter Mater. Phys.* **2007**, *76*, 214115.

(21) Singh, D. J.; Takenaka, H.; Jellison, G. E.; Boatner, L. A. Applications of First Principles Theory to Inorganic Radiation Detection Materials. *MRS Proc.* **2007**, *1038*, 1038-O02-01.

(22) Ning, L.; Yang, F.; Duan, C.; Zhang, Y.; Liang, J.; Cui, Z. Structural Properties and 4f -> 5d Absorptions in Ce-Doped Lualo3: A First-Principles Study. *J. Phys. Condens. Matter* **2012**, *24*, 055502.

(23) Fang, Z.-x.; Ning, L.-x.; Cui, Z.-f. First Principles Study on the 4f-5d Transition of Ce3+ in Lualo3. *Chin. J. Chem. Phys.* **2011**, *24*, 134−140.

(24) Heyd, J.; Scuseria, G. E.; Ernzerhof, M. Hybrid Functionals Based on a Screened Coulomb Potential. *J. Chem. Phys.* **2003**, *118*, 8207−8215.

(25) Perdew, J. P.; Ernzerhof, M.; Burke, K. Rationale for Mixing Exact Exchange with Density Functional Approximations. *J. Chem. Phys.* **1996**, *105*, 9982−9985.

(26) Kresse, G.; Furthmüller, J. Efficiency of Ab-Initio Total Energy Calculations for Metals and Semiconductors Using a Plane-Wave Basis Set. *Comput. Mater. Sci.* **1996**, *6*, 15−50.

(27) Kresse, G.; Furthmüller, J. Efficient Iterative Schemes for Ab Initio Total-Energy Calculations Using a Plane-Wave Basis Set. *Phys. Rev. B: Condens. Matter Mater. Phys.* **1996**, *54*, 11169.

(28) Kresse, G.; Hafner, J. Abinitio Molecular-Dynamics for Liquid-Metals. *Phys. Rev. B: Condens. Matter Mater. Phys.* **1993**, *47*, 558−561.

(29) Blöchl, P. E. Projector Augmented-Wave Method. *Phys. Rev. B: Condens. Matter Mater. Phys.* **1994**, *50*, 17953−17979.

(30) Kresse, G.; Joubert, D. From Ultrasoft Pseudopotentials to the Projector Augmented-Wave Method. *Phys. Rev. B: Condens. Matter Mater. Phys.* **1999**, *59*, 1758−1775.

(31) Perdew, J. P.; Burke, K.; Ernzerhof, M. Generalized Gradient Approximation Made Simple. *Phys. Rev. Lett.* **1996**, *77*, 3865−3868.

(32) Dudarev, S. L.; Botton, G. A.; Savrasov, S. Y.; Humphreys, C. J.; Sutton, A. P. Electron-Energy-Loss Spectra and the Structural Stability of Nickel Oxide: An Lsda+U Study. *Phys. Rev. B: Condens. Matter Mater. Phys.* **1998**, *57*, 1505−1509.

(33) Dujardin, C.; Pedrini, C.; Gâcon, J. C.; Petrosyan, A. G.; Belsky, A. N.; Vasil'ev, A. N. Luminescence Properties and Scintillation Mechanisms of Cerium- and Praseodymium-Doped Lutetium Orthoaluminate. *J. Phys. Condens. Matter* **1997**, *9*, 5229−5243.

(34) da Silva, E. L.; Marinopoulos, A. G.; Vieira, R. B. L.; Vilao, R. C.; Alberto, H. V.; Gil, J. M.; Lichti, R. L.; Mengyan, P. W.; Baker, B. B. Electronic Structure of Interstitial Hydrogen in Lutetium Oxide from Dft Plus U Calculations and Comparison Study with Mu Sr Spectroscopy. *Phys. Rev. B* **2016**, *94*, 014104.

(35) Dorado, B.; Amadon, B.; Freyss, M.; Bertolus, M. Dft Plus U Calculations of the Ground State and Metastable States of Uranium Dioxide. *Phys. Rev. B: Condens. Matter Mater. Phys.* **2009**, *79*, 235125.

(36) Meredig, B.; Thompson, A.; Hansen, H. A.; Wolverton, C.; van de Walle, A. Method for Locating Low-Energy Solutions within Dft Plus U. *Phys. Rev. B: Condens. Matter Mater. Phys.* **2010**, *82*, 195128.

(37) Krukau, A. V.; Vydrov, O. A.; Izmaylov, A. F.; Scuseria, G. E. Influence of the Exchange Screening Parameter on the Performance of Screened Hybrid Functionals. *J. Chem. Phys.* **2006**, *125*, 224106.

(38) Kolobanov, V.; Mikhailin, V.; Petrovnin, N.; Spassky, D.; Zorenko, Y. Exciton Creation in Lualo3 Single Crystalline Film. *Phys. Status Solidi B* **2006**, *243*, R60−R62.

(39) Komsa, H. P.; Broqvist, P.; Pasquarello, A. Alignment of Defect Levels and Band Edges through Hybrid Functionals: Effect of Screening in the Exchange Term. *Phys. Rev. B: Condens. Matter Mater. Phys.* **2010**, *81*, 205118.

(40) Thomas, B. S.; Marks, N. A.; Begg, B. D. Defects and Threshold Displacement Energies in Srtio(3) Perovskite Using Atomistic Computer Simulations. *Nucl. Instrum. Methods Phys. Res., Sect. B* **2007**, *254*, 211−218.

(41) Uberuaga, B. P.; Vernon, L. J. Interstitial and Vacancy Mediated Transport Mechanisms in Perovskites: A Comparison of Chemistry and Potentials. *Solid State Ionics* **2013**, *253*, 18−26.

(42) Liu, B.; Xiao, H. Y.; Zhang, Y.; Aidhy, D. S.; Weber, W. J. Ab Initio Molecular Dynamics Simulations of Threshold Displacement Energies in Srtio3. *J. Phys. Condens. Matter* **2013**, *25*, 485003.

(43) Broberg, D.; Medasani, B.; Zimmermann, N. E. R.; Yu, G.; Canning, A.; Haranczyk, M.; Asta, M.; Hautier, G. Pycdt: A Python

https://dx.doi.org/10.1021/acsami.0c13236
ACS Appl. Mater. Interfaces 2020, 12, 46296−46305

Toolkit for Modeling Point Defects in Semiconductors and Insulators. *Comput. Phys. Commun.* **2018**, *226*, 165−179.
(44) Ong, S. P.; Richards, W. D.; Jain, A.; Hautier, G.; Kocher, M.; Cholia, S.; Gunter, D.; Chevrier, V. L.; Persson, K. A.; Ceder, G. Python Materials Genomics (Pymatgen): A Robust, Open-Source Python Library for Materials Analysis. *Comput. Mater. Sci.* **2013**, *68*, 314−319.
(45) Zimmermann, N. E. R.; Horton, M. K.; Jain, A.; Haranczyk, M. Assessing Local Structure Motifs Using Order Parameters for Motif Recognition, Interstitial Identification, and Diffusion Path Characterization. *Front. Mater.* **2017**, *4*, 34.
(46) Medasani, B.; Sushko, M. L.; Rosso, K. M.; Schreiber, D. K.; Bruemmer, S. M. First-Principles Investigation of Native Interstitial Diffusion in Cr2o3. *J. Phys. Chem. C* **2018**, *122*, 12984−12993.
(47) Levy, M. R.; Grimes, R. W.; Sickafus, K. E. Disorder Processes in a(3+)B(3+)O(3) Compounds: Implications for Radiation Tolerance. *Philos. Mag.* **2004**, *84*, 533−545.
(48) Vasylechko, L.; Senyshyn, A.; Bismayer, U. Perovskite-Type Aluminates and Gallates. *Handbook on the Physics and Chemistry of Rare Earths*; Elsevier, 2009; Chapter 242, pp 113−295.
(49) Ju, M.; Lu, C.; Yeung, Y.; Kuang, X.; Wang, J.; Zhu, Y. Structural Evolutions and Crystal Field Characterizations of Tm-Doped Yalo3: New Theoretical Insights. *ACS Appl. Mater. Interfaces* **2016**, *8*, 30422−30429.
(50) Tran, F.; Blaha, P. Accurate Band Gaps of Semiconductors and Insulators with a Semilocal Exchange-Correlation Potential. *Phys. Rev. Lett.* **2009**, *102*, 226401.
(51) Choudhary, K.; Zhang, Q.; Reid, A. C. E.; Chowdhury, S.; Nguyen, N. V.; Trautt, Z.; Newrock, M. W.; Congo, F. Y.; Tavazza, F. Computational Screening of High-Performance Optoelectronic Materials Using Optb88vdw and Tb-Mbj Formalisms. *Data Sci.* **2018**, *5*, 180082.
(52) Pilania, G.; McClellan, K. J.; Stanek, C. R.; Uberuaga, B. P. Physics-Informed Machine Learning for Inorganic Scintillator Discovery. *J. Chem. Phys.* **2018**, *148*, 241729.
(53) Bannow, L. C.; Rosenow, P.; Springer, P.; Fischer, E. W.; Hader, J.; Moloney, J. V.; Tonner, R.; Koch, S. W. An Ab Initio Based Approach to Optical Properties of Semiconductor Heterostructures. *Model. Numer. Simul. Mater. Sci.* **2017**, *25*, 065001.
(54) Erhart, P.; Schleife, A.; Sadigh, B.; Aberg, D. Quasiparticle Spectra, Absorption Spectra, and Excitonic Properties of Nai and Sri2 from Many-Body Perturbation Theory. *Phys. Rev. B: Condens. Matter Mater. Phys.* **2014**, *89*, 075132.
(55) Yin, W. J.; Shi, T. T.; Yan, Y. F. Unusual Defect Physics in Ch3nh3pbi3 Perovskite Solar Cell Absorber. *Appl. Phys. Lett.* **2014**, *104*, 063903.
(56) Xu, P.; Chen, S.; Xiang, H.-J.; Gong, X.-G.; Wei, S.-H. Influence of Defects and Synthesis Conditions on the Photovoltaic Performance of Perovskite Semiconductor Cssnl(3). *Chem. Mater.* **2014**, *26*, 6068−6072.
(57) Cooper, M. W. D.; Murphy, S. T.; Andersson, D. A. The Defect Chemistry of Uo2 +/- X from Atomistic Simulations. *J. Nucl. Mater.* **2018**, *504*, 251−260.
(58) Matthews, C.; Perriot, R.; Cooper, M. W. D.; Stanek, C. R.; Andersson, D. A. Cluster Dynamics Simulation of Uranium Self-Diffusion During Irradiation in Uo2. *J. Nucl. Mater.* **2019**, *527*, 151787.
(59) Jain, A.; Ong, S. P.; Hautier, G.; Chen, W.; Richards, W. D.; Dacek, S.; Cholia, S.; Gunter, D.; Skinner, D.; Ceder, G.; Persson, K. A. Commentary: The Materials Project: A Materials Genome Approach to Accelerating Materials Innovation. *APL Mater.* **2013**, *1*, 011002.
(60) Marezio, M.; Remeika, J. P.; Dernier, P. D. Rare Earth Orthogallates. *Inorg. Chem.* **1968**, *7*, 1337−1340.
(61) Dujardin, C.; Pedrini, C.; Blanc, W.; Gâcon, J. C.; van't Spijker, J. C.; Frijns, O. W. V.; van Eijk, C. W. E.; Dorenbos, P.; Chen, R.; Fremout, A.; Tallouf, F.; Tavernier, S.; Bruyndonckx, P.; Petrosyan, A. G. Optical and scintillation properties of large crystals. *J. Phys. Condens. Matter* **1998**, *10*, 3061−3073.

https://dx.doi.org/10.1021/acsami.0c13236
ACS Appl. Mater. Interfaces 2020, 12, 46296−46305